AFRL-AFOSR-VA-TR-2023-0151

Exploring new concepts towards multi-mode low-power robust electric propulsion

Keidar, Michael
THE GEORGE WASHINGTON UNIVERSITY
2121 I ST NW STE 601
WASHINGTON, DC,
US

11/07/2022
Final Technical Report

Air Force Research Laboratory
Air Force Office of Scientific Research
Arlington, Virginia 22203
Air Force Materiel Command

REPORT DOCUMENTATION PAGE

PLEASE DO NOT RETURN YOUR FORM TO THE ABOVE ORGANIZATION.

1. REPORT DATE	**2. REPORT TYPE**	**3. DATES COVERED**	
20221107	Final	**START DATE** 20190401	**END DATE** 20220831

4. TITLE AND SUBTITLE
Exploring new concepts towards multi-mode low-power robust electric propulsion

5a. CONTRACT NUMBER	**5b. GRANT NUMBER**	**5c. PROGRAM ELEMENT NUMBER**
	FA9550-19-1-0166	61102F
5d. PROJECT NUMBER	**5e. TASK NUMBER**	**5f. WORK UNIT NUMBER**

6. AUTHOR(S)
Michael Keidar

7. PERFORMING ORGANIZATION NAME(S) AND ADDRESS(ES)
THE GEORGE WASHINGTON UNIVERSITY
2121 I ST NW STE 601
WASHINGTON, DC
US

8. PERFORMING ORGANIZATION REPORT NUMBER

9. SPONSORING/MONITORING AGENCY NAME(S) AND ADDRESS(ES)	**10. SPONSOR/MONITOR'S ACRONYM(S)**	**11. SPONSOR/MONITOR'S REPORT NUMBER(S)**
Air Force Office of Scientific Research 875 N. Randolph St. Room 3112 Arlington, VA 22203	AFRL/AFOSR RTA1	AFRL-AFOSR-VA-TR-2023-0151

12. DISTRIBUTION/AVAILABILITY STATEMENT
A Distribution Unlimited: PB Public Release

13. SUPPLEMENTARY NOTES

14. ABSTRACT
George Washington University developed multi-mode low-power electric propulsion. In particular high thrust to power ratio and efficiency in low power regimes (< 30W) were achieved. This work resulted in development a new device for CubeSatellite propulsion called two-stage micro-cathode arc thruster. Being magnetized by an axially symmetric dc magnetic field, the vacuum arc discharge demonstrates a threshold behavior: parameters such as thrust and the thrust-to-power ratio rapidly jump after a certain dc voltage. It is demonstrated that such an effect improves the thrust (over 1 mN), efficiency (about 50%), and thrust-to-power ratio (over 30 Î¼N/W).

15. SUBJECT TERMS

16. SECURITY CLASSIFICATION OF:			**17. LIMITATION OF ABSTRACT**	**18. NUMBER OF PAGES**
a. REPORT	**b. ABSTRACT**	**c. THIS PAGE**		
U	U	U	UU	17

19a. NAME OF RESPONSIBLE PERSON	**19b. PHONE NUMBER** *(Include area code)*
MITAT BIRKAN	426-7234

Exploring new concepts towards multi-mode low-power robust electric propulsion

Michael Keidar
George Washington University, Washington DC

Lubos Brieda
Particle in Cell Consulting LLC

Final Report

Abstract: George Washington University in collaboration with PIC consulting is working on multi-mode low-power electric propulsion. In particular we are focusing on achieving high thrust to power ratio and efficiency in low power regimes (< 30W). This is an important issue in micropropulsion since most microthrusters have low efficiency limiting their applications. This work resulted in development a new device for CubeSatellite propulsion called two-stage micro-cathode arc thruster. Being magnetized by an axially symmetric dc magnetic field, the vacuum arc discharge demonstrates a threshold behavior: parameters such as thrust and the thrust-to-power ratio rapidly jump after a certain dc voltage. It is demonstrated that such an effect improves the thrust (over 200 μN), efficiency (about 50%), and thrust-to-power ratio (about 20 μN/W).

1.High-thrust to power ratio microthruster

Further progress in space satellites technologies is highly associated with a decrease of satellites launch cost, which is directly proportional to satellite mass and size. This has led to the miniaturization of satellites as a design trend in the space industry (*1*). Minute electric propulsion subsystems seem to be the most perspective since they use electromagnetic plasma acceleration to create high exhaust speed (therefore, high efficiency with less propellant storage onboard), and they also provide a convenient way to control the thruster parameters over a wide-range by varying the electrical power level (*2*). One of the most mature and widely-used electric propulsion technologies is the Hall thruster which uses xenon as a propellant. Even operating at low (60 – 270 W) power suitable for propulsion of small satellites, such thrusters provide sufficient range of thrusts (from 5 to 25 mN) at a specific impulse of about 400 – 1800 s and high thrust-to-power ratio (TPR) of about 65 μN/W (*3*). However, xenon is very expensive rare noble gas with a worldwide production limited only about 50-60 tons (*4*), and therefore xenon-based electric propulsion has to compete with other fields of industry (imaging & lighting, electronics & semiconductor industry (*5*), medicine (*6*) etc.) for xenon consumption. A promising new electric propulsion design for small satellites is the micro-cathode vacuum arc thrusters (μCATs). Their key advantage is that they use a propellant stored as a solid – a state of matter with the highest atomic density, which can be stored much more efficiently than liquid or gaseous propellant. Its solid electrodes can be made of widespread and relatively cheap metals as copper or titanium. During the μCAT thruster firing, a solid converts into plasma which can be further accelerated by electromagnetic fields. Despite the other miniature electrical thrusters with solid propellant (such as an iodine thruster (*7*)), μCATs do not use toxic propellants, and they do not have a warm-up time, i.e. they can be ignited instantly after providing the respective control signal. The μCATs performance has been successfully demonstrated in flight tests during BRICSat, CANYVAL-X,

and BRICSat-P missions (*8-10*). Typical thrust T and specific impulse I_{sp} levels for μCATs are within 50 μN and 3000 s, with a TPR of less than 4 μN/W at 1-15 W power (*10*). The challenge for this design is that for some applications such as orbit raising maneuvers, a much higher thrust value is needed. Also, the power and propellant storage limitations on small satellites require higher values of TPR and energetic efficiency. Recent tests on design modifications of this thruster (*11*) demonstrated that adding a second MPD stage to μCAT allows the thruster to simultaneously achieve higher levels of thrust (~210 μN), TPR (~18 μN/W) and efficiency (~50 %). Although it was found (*11*) that after the onset of the magnetized vacuum arc the performance of the two-stage μCAT-MPD thruster rapidly jumps, it was still unclear how will the performance behave with the further increase of the power delivered to the second stage. Effect of the increased mass flow rate due to much more intense ions generation in a powerful second-stage discharge with simultaneous ion acceleration by the Lorentz force, on the specific impulse of the device was also remained unexplored. Therefore, the question regarding accessibility of higher thrust, TPR and efficiency, as well as the relationships between I_{sp} and TPR for this two-stage μCAT-MPD thruster was left beyond the scope of the previous research. We address these critical issues in the present paper.

Materials and Methods: Schematic view of the developed thruster is given in the Fig. 1. The first stage (a single μCAT) had a planar configuration, with a central disc-shape Ti cathode and an outer ring-shape Cu anode, which were both placed on a disc-shape ceramic washer. A ring-shaped (1.27 cm ID, 2.54 mm OD, 1.27 cm length) permanent axially-magnetized magnet with induction of ~0.1 T on its axis was placed behind the ceramic washer providing thermal isolation from the first stage. The ceramic washer surface of the first-stage anode-cathode gap was covered by weakly-conductive carbon paint ensuring initiation trigger-less (*12*) arc discharge with the first-stage pulse duration τ_1, current $I_1(t)$, voltage $U_1(t)$ and the average power P_1. As a second stage, a conical frustum (made of thin molybdenum foil with narrow opening separated by the gap d from the cathode surface) was used. Preliminary plasma from the first stage, due to the dc voltage U_{MPD} between the cathode and the second-stage electrode, initiated more powerful arc discharge in the second stage with the second-stage pulse duration τ_2, current $I_2(t)$, voltage $U_2(t)$ and the average power P_2. The interaction of azimuthal electronic current j_θ, flowing in plasma, with the radial component of the external magnetic field B_r resulted in the formation of the Lorentz force $F_L \sim j_\theta \times B_r$ accelerating the plasma towards the wide opening of the MPD electrode and enhancing the thrust. More information on thruster performance, characterization and thrust measurements can be found in the Supplementary Materials and Methods section.

Results and Discussion: The aforementioned design of the μCAT-MPD thruster allowed achieving the performance parameters that are superior to many known propulsion devices operating at comparable power levels (Fig. 2). Figure 2 (**a**) demonstrates that the gap between the first and second stages impacts the thrust level: a lower gap generates higher thrust values, while a zero gap (when the second-stage electrode becomes the part of the anode and acquires its potential) generates a fixed value of ~15 μN and cannot be throttled. At the optimal (short) gap, the thrust incrementally grows (within three orders of magnitude!) with the total power $P = P_1 + P_2$ determined by U_{MPD}, and finally reaches 1.7 mN. Note that the thrust growth rate with U_{MPD} doesn't show any saturation at high U_{MPD}: thus it appears physically possible to have higher thrust values if the second-stage voltage is increased further. Also note that the thrust grows faster than the power, so TPR also grows incrementally and reaches 37.4 μN/W (for the case of a short gap). The power dissipated in both stages of the thruster is given in the Fig. 2 (**b**, **c**). Extraction of high ionic currents with activated second stage leads to only moderate increase of the power dissipated in the first stage, while the first-stage discharge burning voltage grows mainly to the magnetization

of the plasma electrons (*11*). We can see from Fig. 2 (**b**) that both – the first and the second stage – powers grow with U_{MPD}, however, this trend is much stronger for P_2 rather than for P_1. Despite this growth, the total power P still remains relatively low – below 50 W (Fig. 2, **c**), which indicates that such thruster still can be considered as a low-power device. Figure 2(**d**) demonstrates that for any non-zero gap between the thruster stages, the exhausting ion velocity does not change significantly with the increase of the U_{MPD} voltage. This indicates that the specific impulse I_{sp} of the thruster doesn't degrade significantly with a proportional growth in thrust with the U_{MPD}. Since the thruster demonstrates the highest performance with short gap (Fig. 2, a), the experimental results below are given for the 'short gap' case only. The photos obtained by an ICCD camera demonstrate that plasma plume during the discharge firing is directed from the first-stage cathode toward the thruster exhaust mostly inside the volume of the cone, not from its side.

The fractions of pulse-average total current $\langle I_i \rangle$ and charge $\langle Q_i \rangle$ of ions expelled by the thruster (Fig. 4, **a**) demonstrate that the thruster produces and expels more ions for the same amount of discharge currents in both stages with the increase of U_{MPD}. Images of the cathodes with the traces of the cathodic spots (Fig. 4, **b**, **c**) demonstrate that the activation of discharge in the second stage leads to significant expansion of the erosion area in comparison with the case when the plasma is produced by the first stage only.

Results in the Fig. 4 (**b**, **c**) indicate that the preliminary plasma, produced by the first stage from a tiny area occupied by cathode spots, leads to the formation of the large-area cathode spots after supplying second-stage voltage. The cathode spot area shown on Fig. 4, **b** was produced by relatively short arc pulse (tens of micro-seconds), while the arc duration of the second-stage arc (shown in Fig. 4, **c**) is significantly larger (up to several milliseconds) at pulse-average current up to 9 A. Taking into account that the arc at the second stage was ignited already at background of the relatively dense plasma (~10^{20} m^3) generated at the first stage, the observed change of the cathode spot areas can be understood as result of change in the dynamics of spot behavior and their types. Indeed, according to well-known investigations (*13*), the arc current, arc duration, surrounding plasma (gas) pressure and cathode surface state determine the different spot types, which are characterized by spot lifetime, velocity, spot current and cathode erosion. It was established that spot type changed from fast to slow moving spots with the arc time duration (*13*). At the arc beginning, the fast and short-lived (<10 μs) spots were observed. These cathode spots typically appear at a thin oxide or impurity films and lead to relatively low cathode erosion rate (*14*). On the other hand, the slow-moving spots appear during arc development (100 μs and more), when the cathode is heated locally, and in the near-cathode region a dense plasma exist impeding the cathode plasma flow. As a result, the cathode erosion rate significantly increases with respect to that rate produced by fast spots. The influence of the background plasma with density of ~$10^{20}$$m^3$ on the time of development of the cathode plasma plume was also observed for much longer arc time – from one to few tens of seconds for different cathode materials (*15*). Kimblin (*16*) also demonstrated experimentally the relatively large fraction of ion current for long duration arcs in range of 0.1 – 3 s. These processes explain the increase of the cathode erosion (flow rate) and consequently the thrust-to-power ratio in the case of a two-stage thruster configuration. Aforementioned features of the cathodic spots in the single-stage and two-stage firing regimes manifest themselves also in the different waveforms of the first and second stage currents which finally results in the change of the total ion current waveform (Fig. 5). With the zero second-stage voltage (U_{MPD} = 0 V, Fig. 5, **a**) no current is flowing in the second stage, the total ion current is short and mimics the waveform of the first-stage current. High second-stage voltage (U_{MPD} = 180 V, Fig. 5, **a**) initiates longer second-stage current pulse which results in high amplitude and

duration of the total ion current which waveform now looks like a superposition of the waveforms of both discharge currents.

A more detailed study of the interconnection between TPR and I_{sp} for the thruster with variable position of magnet with respect to the discharge area have revealed an interesting non-monotonous connections between these parameters (Fig. 6, **a**). One can see (Fig. 6, **a**) that the TPR vs. I_{sp} trend has two characteristic regions: decreasing (blue region) and increasing (pink region). In the decreasing part, the highest TPR of 37 μN/W is observed for the highest values of voltage U_{MPD} = 180 V and the total power P = 48.8 W. This decreasing part of TPR vs. I_{sp} trend can be called "traditional" since it is typical for most of the propulsion devices working within broad range of thrust, TPR and power levels (Fig. 6, **b**). The other ('anomalous') region at higher I_{sp}, which has the growing TPR vs. I_{sp} trend, has not been observed before for any other device in the literature (Fig. 6, **b**). Comparison of 'TPR vs. I_{sp}' with 'Mass flow rate vs. I_{sp}' trends provides additional argument to support the claim that the main physical reason for the growth of TPR is the increase of mass flow rate at the same power: these two trends match each other (Fig. 6, **a**).

Although the problem of production of macroparticles in vacuum arc discharges is well-known, we think that these particles do not contribute significantly to the generated thrust in our thruster due to the following reasons. Ion erosion rate E_r, which we estimated as $E_r = \alpha_i M_i / e\bar{Z}$ (where $\alpha_i = Q_i/(Q_1+Q_2)$ is the normalized integral of total ion current, M_i is the atomic mass of cathode material, e is elementary charge and $\bar{Z}$ is the mean charge state of the ion) and plotted in the Fig. 6, **a**, was found to be lower or comparable with the erosion rates from the literature for Ti (22.4 μg/C) or Cu (33.4 μg/C) cathodes (*17*). Accounting for the microparticles may increase the cathode erosion rate; however, as follows from Daalder (*18*), their production becomes noticeable only after reaching the high values (about 1 C) of the discharge current integral at high current amplitudes (around hundreds of amperes) and pulse durations (around seconds), which is not the case of our thruster. Additionally, magnetic field causes the motion of the cathodic spot over the cathode surface which, in turn, decreases the local thermal loads on the cathode and finally minimizes the generation of macroparticles (*19*). Moreover, these macroparticles typically have much lower velocities (10^2-10^3 m/s, *20-22*) than ions (several km/s).

The presence of the "traditional" and "anomalous" 'TPR vs. I_{sp}' trends can be explained by the fact that the exhausting ion velocity of the μCAT-MPD thruster depends on the magnetic field strength and configuration. In a case of permanent magnet, it can be regulated by the position z of the magnet with respect to the second stage (Fig. 7, **a**). Fig. 7 (**a**) demonstrates that when z is short, the radial component of the magnetic field B_r reaches a value high enough for a significant contribution of Lorentz force to ion acceleration, and therefore the ion velocity grows with the second-stage voltage U_{MPD}. However, increasing the distance between the magnet and the second stage results in a more moderate growth of ion velocities, and finally, when the magnet is far enough (z = 37 mm), the ions start to decelerate due to the positive second-stage potential, with the second-stage discharge attempting to switch into uncontrollable dc mode.

One can see that generally ion velocities in the Fig. 7 (**a)** are lower than in the Fig. 2 (**d**). This difference comes from the cathode material: the ions ejected from the titanium cathode (Fig. 2, **d**) typically have narrow velocity distribution with a peak around 17 km/s and high-velocity tail up to 24 km/s (*26*), while the copper cathode (Fig. 7, **a**) expels heavier ions with quite broad distribution of initial ion velocities from 9 km/s with the peak around 13-15 km/s (*26*, *27*). Nevertheless, the data in the Fig. 7 (**a**) allows notice the effect of the magnetic field on the ions acceleration: even at U_{MPD} = 0, the ion velocity is higher when the magnet locates closer to the discharge area, justifying that the ions accelerate due to magnetic mirror effect (*27*, *28*). Additional

source of ions acceleration comes from the Lorentz force $F_L \sim j_\theta \times B_r$ which makes contribution to thrust at higher values of the magnetic field in the vicinity of discharge region and discharge currents (and correspondingly, electron currents in plasma). Previous simulations of contribution of F_L to thrust (*11*) showed us that the $j_\theta \times B_r$ acceleration region has a typical length of within 1 mm, so the contribution of Lorentz force to thrust can be comparable with the initial thrust (*29*) and strongly depends on the magnetic field strength and configuration defined by the position of the magnet with respect to the discharge area.

These results demonstrate that such two-stage μCAT-MPD thruster has another independent "knob" for controlling its performance – namely, the position of the magnet with respect to the discharge region. For the on orbit application of the thruster, instead of moving the permanent magnet, more practical approach can be implemented for the change of the magnetic field strength and configuration – by varying the absolute values and relative ratios of the currents I_1, I_2 feeding two independent electromagnetic coils with cores (Fig. 7, **b**).

Low-power vacuum arc thrusters have the known problem of a limited lifetime, which may vary from 10^3-10^4 pulses (*30*) to 10^5 pulses (*31*), while the special constructions with the cathode feeding mechanism allow achieve several million pulses *(32)*. In our previous study (*33*) we found that the lifetime of the μCAT firing in the high-power regime can be extended to more than one million pulses by the optimizing the anode-cathode gap (extending it to around 1 mm) and providing the magnetic field causing the movement of cathodic spot along the cathode surface. So the configuration of the first-stage electrodes of the newly-designed μCAT-MPD thruster was chosen to provide the maximal lifetime even at the high-power performance.

To conclude, the newly-designed configuration of μCAT-MPD thruster achieves a superior combination of performance parameters: thrust (up to 1.7 mN), together with TPR (up to 37 μN/W), consuming electrical power below than 50 W and efficiency (up to 57 %). The TPR values achieved are superior for low-power devices used for electric propulsion on small satellites and even comparable to the values for more powerful and mature technologies (Fig. 6). Such advantages of vacuum arcs as the almost 100% degree of ionization in plasmas, as well as the very nature of the cathodic spot having almost infinite emission of the charged particles (*34*), speak to the expectation of even higher values of performance parameters of such devices that may be achieved with the future progress of their technology.

References and Notes

1. I. Levchenko, M. Keidar, J. Cantrell, Y.-L. Wu, H. Kuninaka, K. Bazaka, S. Xu, Explore space using swarms of tiny satellites. *Nature* **562**, 185–187 (2018). https://doi.org/10.1038%2Fd41586-018-06957-2

2. I. Levchenko, S. Xu, G. Teel, D. Mariotti, M. L. R. Walker, M. Keidar, Recent progress and perspectives of space electric propulsion systems based on smart nanomaterials. *Nature Communications* **9** Article number: 879 (2018). https://doi.org/10.1038/s41467-017-02269-7.

3. I. Levchenko, S. Xu, S. Mazouffre, D. Lev, D. Pedrini, D. Goebel, L. Garrigues, F. Taccogna, K. Bazaka, Perspectives, frontiers, and new horizons for plasma-based space electric propulsion. *Physics of Plasmas* **27** 020601 (2020). https://doi.org/10.1063/1.5109141.

4. Xenon Market Size, Share&Covid-19 Impact Analysis, By Application (Imaging and Lighting, Medical, satellite, Electronics&Semiconductors, and others (including R&D), and Regional

Forecast, 2020–2027. [(accessed on 29 April 2022)]; Available online: https://www.fortunebusinessinsights.com/xenon-market-101965.

5. J. Son, J. Kwon, S. Kim, Y. Lv, J. Yu, J.-Y. Lee, H. Ryu, K. Watanabe, T. Taniguchi, R. Garrido-Menacho, N. Mason, E. Ertekin, P. Y. Huang, G.-H. Lee, A.M. van der Zande, Atomically precise graphene etch stops for three dimensional integrated systems from two dimensional material heterostructures. *Nature Communications* **9**, Article number: 3988 (2018). https://doi.org/10.1038/s41467-018-06524-3.
6. A.E. Neice, M.H. Zornow, Xenon anesthesia for all, or only a select few? *Anaesthesia* **71**, 1267–1272 (2016). https://doi.org/10.1111/anae.13569.
7. D. Rafalskyi, J. Martínez Martínez, L. Habl, E. Zorzoli Rossi, P. Proynov, A. Boré, T. Baret, A. Poyet, T. Lafleur, S. Dudin, A. Aanesland, In-orbit demonstration of an iodine electric propulsion system. *Nature* 599, 411-424 (2021). https://doi.org/10.1038/s41586-021-04015-y.
8. S. Hurley, G. Teel, J. Lukas, S. Haque, M. Keidar, C. Dinelli, J. Kang, Thruster subsystem for the United States Naval Academy's (USNA) Ballistically Reinforced Communication Satellite (BRICSat-P). *Trans. Japan Soc. Aeronaut. Space Sci. Aerosp. Technol. Japan* **14** Pb157–Pb163 (2016). https://doi.org/10.2322/tastj.14.Pb_157.
9. J.-P. Park, S. Park, K. Lee, H.J. Oh, K.Y. Choi, Y.B. Song, J.-C. Yim, E. Lee, S.-H. Hwang, S.W. Kim, S.J. Kang, M.-S. Kim, S. Jin, S.H. Lee, S.H. Kwon, D.S. Lee, W.-H. Cho, J.-H. Park, S.-W. Yeo, J.-W. Seo, K.B. Lee, S.-H. Lee, J.-H. Yang, G. N. Kim, J. Lee, Y.W. Kim, T.-H. Kim, Cubesat development for CANYVAL-X mission, paper presented at the SpaceOps Conferences (Daejeon, Korea, 16–20 May 2016). https://doi.org/10.2514/6.2016-2493.
10. J.T. King, J. Kolbeck, J.S. Kang, M. Sanders, M. Keidar, Performance analysis of nano-sat scale μCAT electric propulsion for 3U CubeSat attitude control. *Acta Astronautica* **178** 722–732 (2021). https://doi.org/10.1016/j.actaastro.2020.10.006.
11. D.B. Zolotukhin, K.P. Daniels, L. Brieda, M. Keidar, Onset of the magnetized arc and its effect on the momentum of a low-power two-stage pulsed magneto-plasma-dynamic thruster. *Physical Review E* **102** (2020) 021203(R). https://doi.org/10.1103/PhysRevE.102.021203.
12. A. Anders, J. Schein, N. Qi, Pulsed vacuum-arc ion source operated with a "triggerless" arc initiation method. *Review of Scientific Instruments* **71**(2), 827-829 (2000). https://doi.org/10.1063/1.1150305.
13. I.I. Beilis, *Plasma and Spot Phenomena in Electrical Arcs* (Switzerland, AG, Springer Nature, Vol. 1 and 2, 2020).
14. I.I. Beilis, Vacuum Arc Cathode Spot Theory: History and Evolution of the Mechanisms. *IEEE Trans. Plasma Sci.* **47**(8), 3412-3433 (2019). https://doi.org/10.1109/TPS.2019.2904324.
15. I.I. Beilis, Y. Koulik, R.L. Boxman, D. Arbilly, Thin film deposition using a plasma source with a hot refractory anode vacuum arc. *J. Mater Sci.* **45**, 6325–6331 (2010), https://doi.org/10.1007/s10853-010-4452-1.
16. C.W. Kimblin, Erosion and ionization in the cathode spot regions of vacuum arcs. *J. Appl. Phys.* **44**(7) 3074-3081 (1973). https://doi.org/10.1063/1.1662710.

17. A. Anders, E.M. Oks, G.Yu. Yushkov, K.P. Savkin, I.G. Brown, A.G. Nikolaev, Measurements of the Total Ion Flux From Vacuum Arc Cathode Spots. *IEEE Transactions on Plasma Science* **33**(5) 1532-1536 (2005), https://doi.org/10.1109/TPS.2005.856502.

18. J.E. Daalder, Erosion and the origin of charged and neutral species in vacuum arcs. *J. Phys. D: Appl. Phys.* **8**(14) 1647-1659 (1975), https://doi.org/10.1088/0022-3727/8/14/009.

19. S.K. Sethuraman, P.A. Chatterton, A study of the erosion rate of vacuum arcs in a transverse magnetic field. *Journal of Nuclear Materials* **111-112** 510-516 (1972), https://doi.org/10.1016/0022-3115(82)90257-4.

20. T. Utsumi, J.H. English, Study of electrode products emitted by vacuum arcs in form of molten metal particles. *Journal of Applied Physics* **46**(1) 126-131 (1975), https://doi.org/10.1063/1.321333.

21. S. Shalev, S. Goldsmith, R.L. Boxman, In Situ Determination of Macroparticle Velocities in a Copper Vacuum Arc. *IEEE Transactions on Plasma Science* **11**(3) 146-151 (1983), https://doi.org/10.1109/TPS.1983.4316242

22. S. Shalev, R.L. Boxman, S. Goldsmith, Velocities and emission rates of cathode-produced molybdenum macroparticles in a vacuum arc. *Journal of Applied Physics* **58**(7) 2503-2507 (1985), https://doi.org/10.1063/1.335927.

23. K. Holste, P. Dietz, S. Scharmann, K. Keil, T. Henning, D. Zschätzsch, M. Reitemeyer, B. Nauschütt, F. Kiefer, F. Kunze, J. Zorn, C. Heiliger, N. Joshi, U. Probst, R. Thüringer, C. Volkmar, D. Packan, S. Peterschmitt, K. -T. Brinkmann, H.-G. Zaunick, M. H. Thoma, M. Kretschmer, H. J. Leiter, S. Schippers, K. Hannemann, P. J. Klar, Ion thrusters for electric propulsion: Scientific issues developing a niche technology into a game changer, *Review of Scientific Instruments* **91** 061101 (2020). https://doi.org/10.1063/5.0010134.

24. M. Peukert and B. Wollenhaupt, "OHB-System's view on electric propulsion needs," in Presentation, EPIC Workshop, Brussels, Belgium, 2014.

25. B. Wollenhaupt, M. Peukert, R. Gabrielli, Comparison of mission needs with available electric propulsion technologies, paper presented at the Space Propulsion Conference, Rome, Italy, 2016.

26. E. Byon, A. Anders, Ion energy distribution functions of vacuum arc plasmas. *Journal of Applied Physics* **93**(4) 1899-1906 (2003), https://doi.org/10.1063/1.1539535.

27. A. Anders, G.Y. Yushkov, Ion flux from vacuum arc cathode spots in the absence and presence of a magnetic field. *Journal of Applied Physics* **91**(8), 4824-4832 (2002), https://doi.org/10.1063/1.1459619.

28. F.F. Chen, *Plasma Physics and Controlled Fusion* (Plenum, New York, 1984).

29. D.B. Zolotukhin, K.P. Daniels, S.R.P. Bandaru, M. Keidar, Magnetoplasmadynamic two-stage micro-cathode arc thruster for CubeSats. *Plasma Sources Science and Technology* **28**(10) 105001 (2019). https://doi.org/10.1088/1361-6595/ab4170.

30. J. Lun, C. Law, Direct thrust measurement stand with improved operation and force calibration technique for performance testing of pulsed micro-thrusters. *Measurement Science and Technology* **25**(9), 095009 (2014), http://dx.doi.org/%2010.1088/0957-0233/25/9/095009.

31. I. Kronhaus, K. Schilling, M. Pietzka, J. Schein, Simple orbit and attitude control using vacuum arc thrusters for picosatellites. *J. Spacecr. Rockets* **51**(6), 2008-2015 (2014), https://doi.org/10.2514/1.A32796.

32. I. Kronhaus, M. Laterza, Y. Maor, Inline screw feeding vacuum arc thruster. *Rev. Sci. Instrum.* **88**(4), 043505 (2017), https://doi.org/10.1063/1.4979706.

33. D.B. Zolotukhin, M. Keidar, Optimization of discharge triggering in micro-cathode vacuum arc thruster for CubeSats. *Plasma Sources Sci. Technol.* **27**(7) 074001 (2018), https://doi.org/10.1088/1361-6595/aacdb0.

34. J.M. Lafferty, *Vacuum Arcs: Theory and Applications* (Wiley, 1980).

35. D.B. Zolotukhin, A.V. Tyunkov, Yu.G. Yushkov, E.M. Oks, M. Keidar. Improvement of micro-cathode arc thruster lifetime by deposition of boron-containing coating, *Journal of Propulsion and Power* **36**(5) 744-751 (2020). https://doi.org/10.2514/1.B37790.

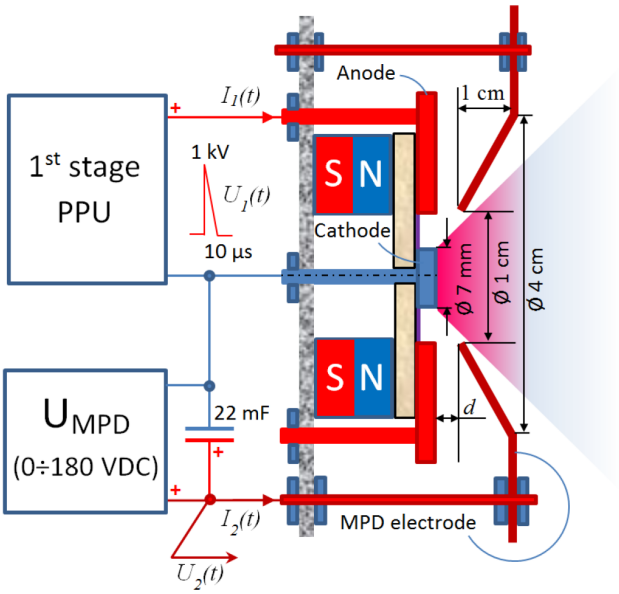

Fig. 1. Schematic of the µCAT-MPD thruster. Preliminary plasma, generated by an arc discharge between cathode and anode of the first stage, initiates a more powerful arc discharge between the second-stage conical MPD electrode and the cathode. Then, the interaction of azimuthal electronic current in the second-stage plasma and the radial component of magnetic field accelerates the plasma and generates the thrust.

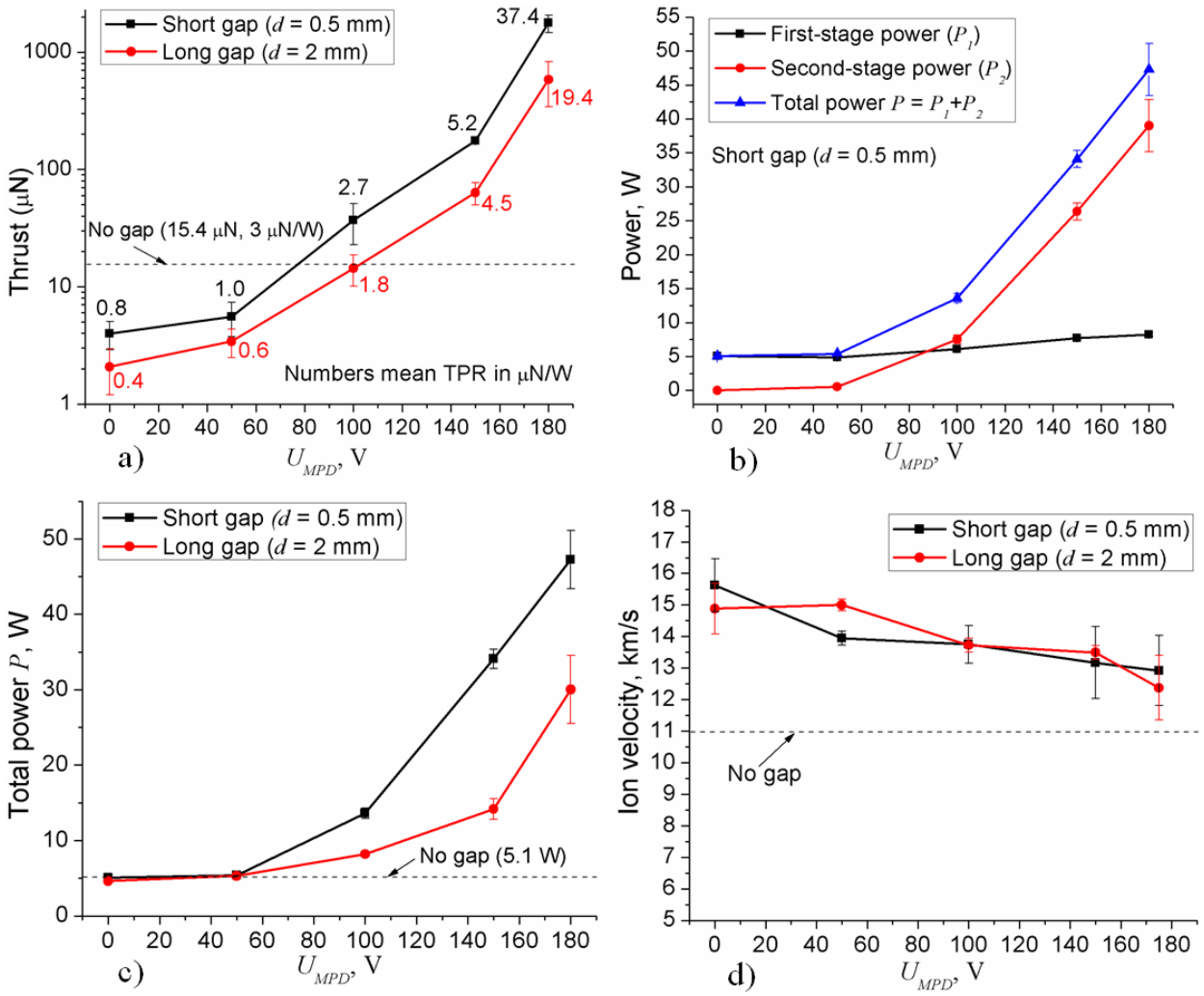

Fig. 2. Experimental results of the μCAT-MPD thruster performance characterization: thrust (a), power in both stages for the short gap (b), total power for the long and short gaps (c), and ion velocity (d) versus the second (MPD) stage voltage U_{MPD}.

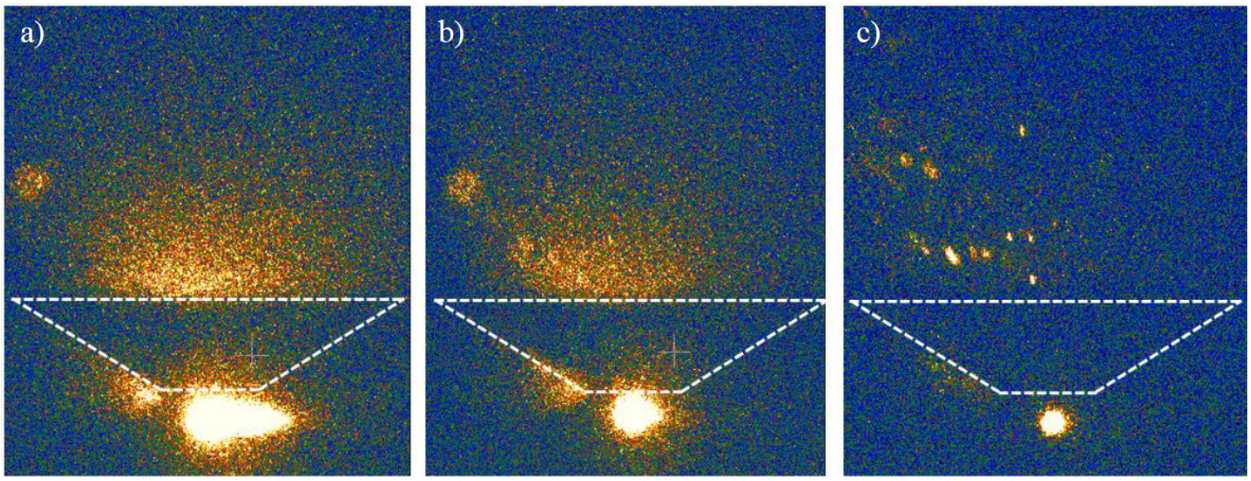

Fig. 3. An image of the plasma plume captured at (a) the moment of the maximal current in the first stage, (b) 240 μs and (c) 370 μs later this maximum. Exposure time 10 μs, white dashed contour represents the approximate boundaries of the second-stage electrode.

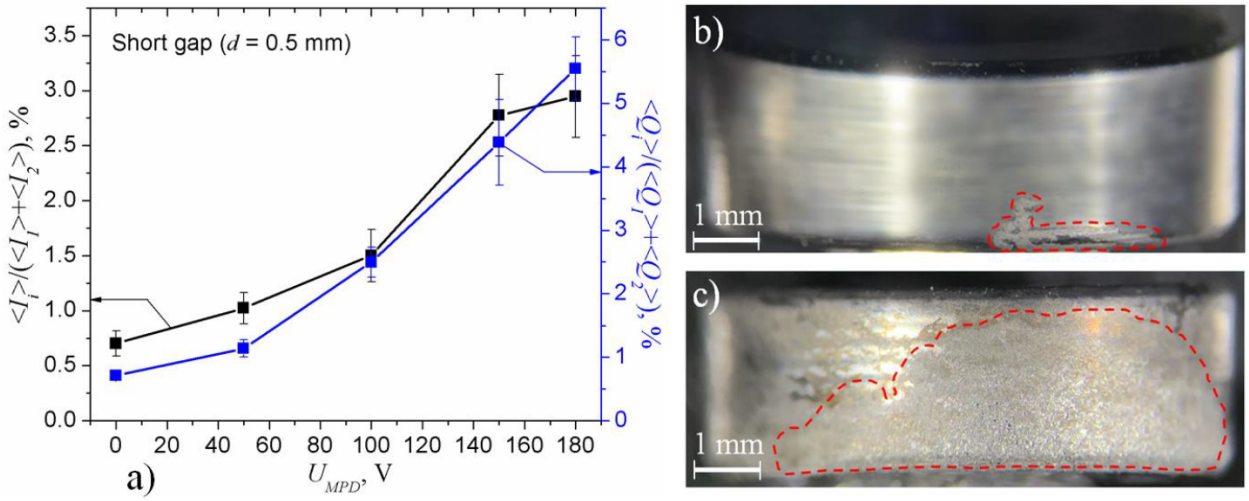

Fig. 4. (a) The ratios of pulse-averaged total current (left axis) and charge (right axis) of ions exhausting by the thruster, to the respective sums of pulse-averaged discharge currents and charges in both stages; Images of the side surfaces of the cathodes after firing of the first stage only (b), and together with the second stage (c) within single pulse. The

image in the Fig. 4 (b) outside the dashed region was blurred in order to focus the attention on the significant details of the surface; original image can be seen in the Fig. S3.

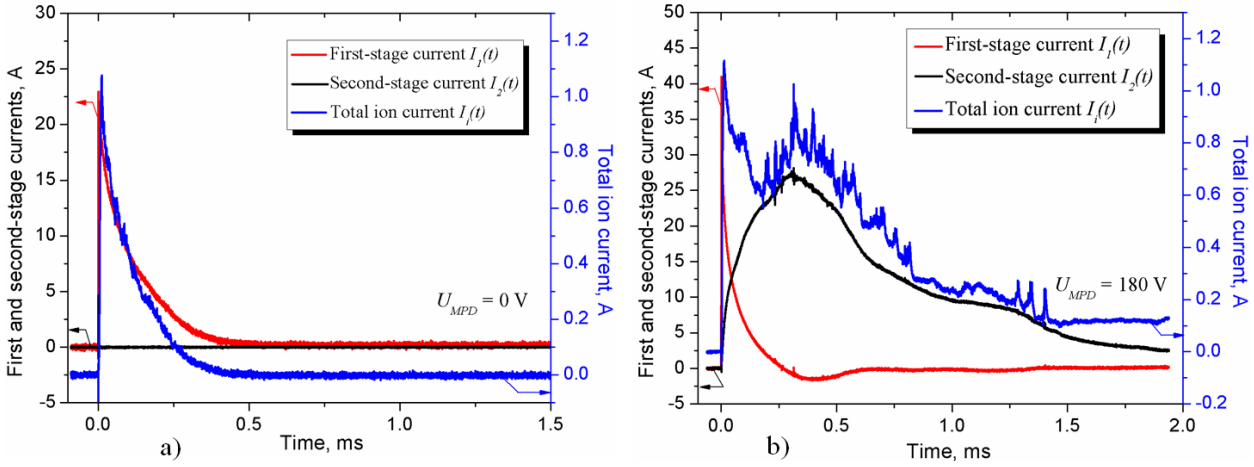

Fig. 5. Temporal characteristics of the first- and second-stage currents as well as the total current of exhausting ions for the two-stage μCAT-MPD thruster with zero (a) and maximal (U_{MPD} = 180 V) voltage on the second stage.

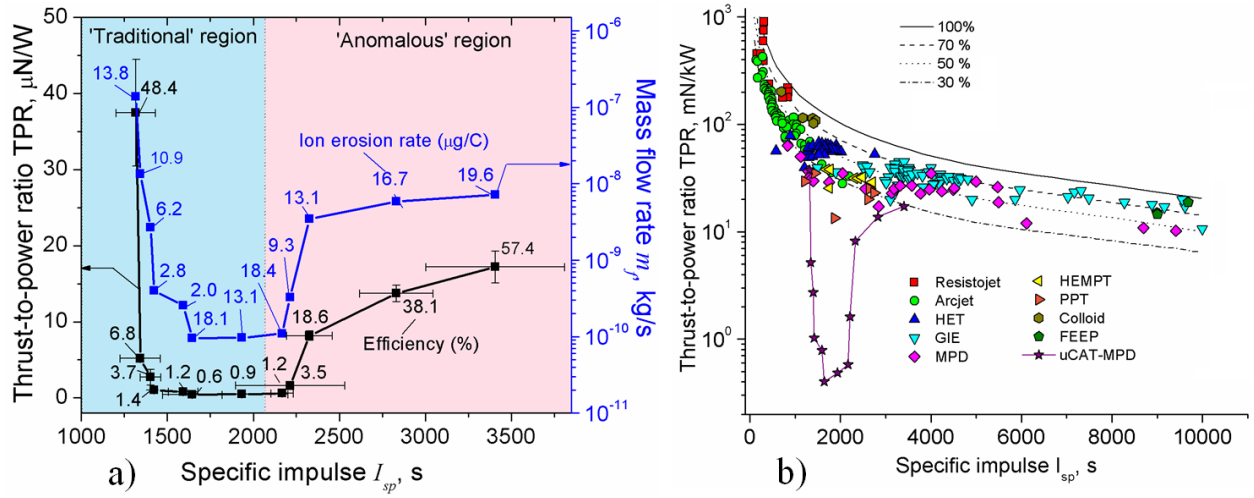

Fig. 6. a) The trends of TPR (left axis) and mass flow rate (right axis) versus the Isp, for the two-stage μCAT-MPD thruster with the planar electrodes, movable magnet and the short gap between the first and second stages; b) TPR vs. Isp trends for different approaches of the powerful thrusters [23-25]: HET – Hall effect thruster, GIE – gridded ion engine, MPD – magnetoplasmadynamic thruster, HEMPT – high efficiency multistage plasma thruster, PPT – pulsing plasma thruster, FEEP – field-emission electric propulsion, μCAT-MPD –

micro-cathode arc thruster with MPD stage (this work). Black curves mean the trends for the fixed values of the efficiency (100 % – 30 %).

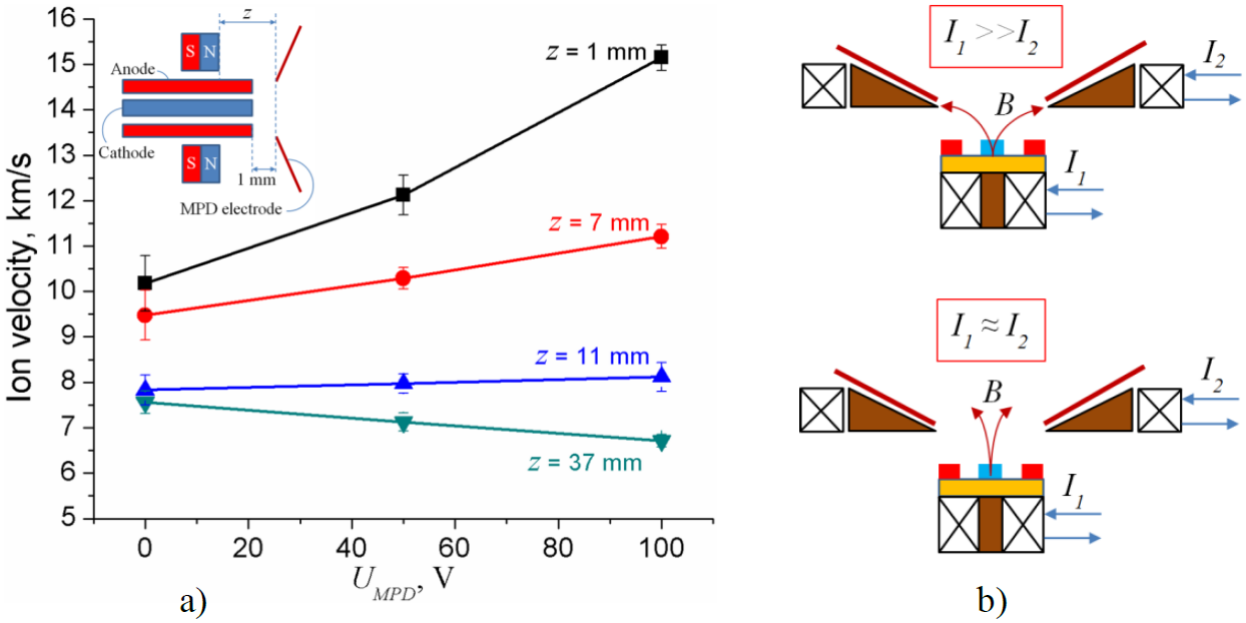

Fig. 7. a) Ion velocity for the two-stage μCAT-MPD thruster with the cylindrical copper cathode and anode, versus the distance z between the magnet face and the opening of the second-stage MPD electrode; b) sketch demonstrating the possibility to control the modulus and direction of the magnetic field strength by the two independent electromagnetic coils with cores.

2.Analysis of Ionization Processes in Air-Breathing Plasma Thruster

Recently, there have been a keen interest in research and development of air-breathing plasma thruster (ABPT) for very low earth orbit applications, typically in range 80-250 km. ABPT uses incoming air as fuel that is ionized and then consequently is accelerated to produce thrust. Typically thrust level is required to cancel drag that is substantial at those low altitudes. There are many advantages but also design and operational challenges when dealing with an ABPT, that is to be addressed. An application of an air-breathing plasma thruster engine is for satellite propulsion and the ability to fly in very low earth orbits, using atmospheric gas molecules. This creates an extended service lifetime. The major challenge is to build an optimum design that can operate in a rarefied gaseous environment within an altitude range of 80-250 km.

The primary focus of this work is to study the ionization in the scramjet-type air-breathing plasma thruster (ABPT) in low earth orbit applications. For a scramjet-type scheme to work, a high degree of ionization needs to be achieved. This paper focuses on plasma chemistry simulation for air in the low earth orbits (80-110 km), to explore the possibility for high ionization of incoming air. The plasma chemistry simulation was performed for air and the variation of ionization degree and species densities were observed concerning the mean input energy that contributes to the chemical reactions. In addition, concept of ABPT without neutralizer has been considered.

3.Discharge characteristics of two-stage micro-cathode arc MPD thrusters with permanent magnet and pulsed magnetic field

Small, light-weight low-power micro-cathode arc thrusters (μCATs) with micro-newton thrust level are well-suitable for altitude control of small satellites like CubeSats. However, for some applications their thrust level needs to be improved which can be done by the adding a second acceleration stage. Recently, we proposed a possible approach for the two-staged thruster – a micro cathode thruster with magneto plasma dynamical (MPD) stage with external magnetic field created by permanent magnet or magnetic coil as shown in Fig 4. Such a two-stage μCAT-MPD concept implies the preliminary production of initial fully-ionized metal plasma by the first stage based on pulsed vacuum arc, and acceleration of this plasma by the j x B force created in the second stage. In this article we discuss some discharge features that such μCAT-MPD thruster experiences in the each configuration of the magnetic field – formed with either a permanent magnet, or a pulsed magnetic coil.

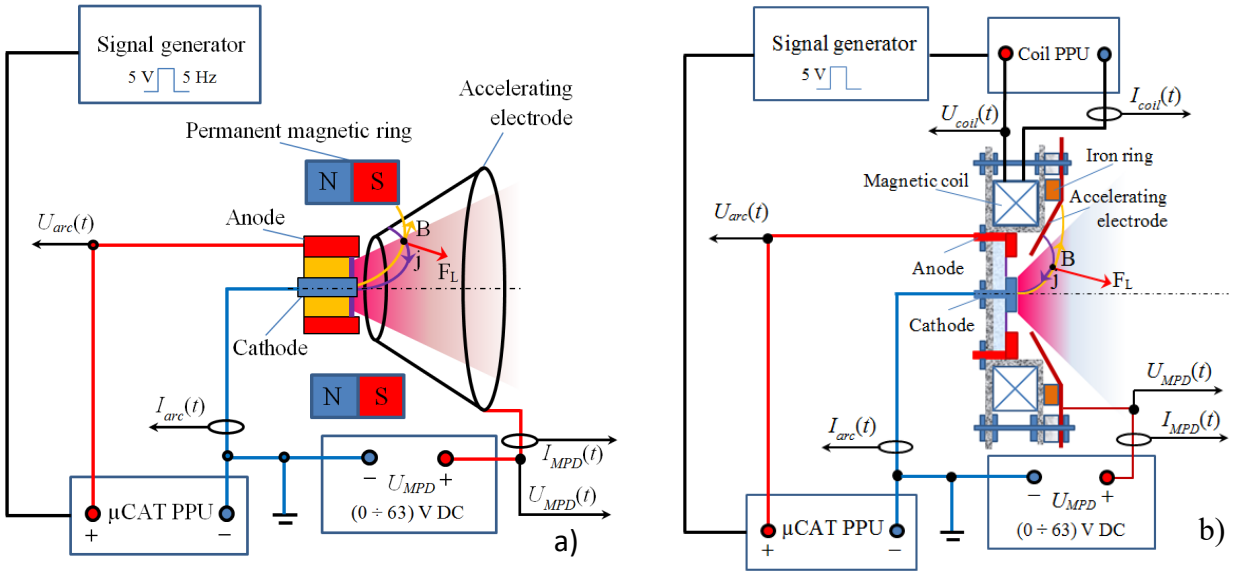

Fig. 4. Schematics of μCAT-MPD thruster with permanent magnetic ring (a), and pulsing magnetic coil (b).

4.DEM Modeling

A DEM-like simulation was set up to simulate cathode erosion and insulator deposition on a 3D domain approximating the flat plates configuration studied previously. These simulations use spherical grains acting on each other with linear $F=kx$ attractive and repulsive spring force. A Maxwellian ion source was included with ions particle impacting momentum onto the grains. Even with this simple setup, we actually get an interesting and realistically-looking behavior, see Figure 5. We can see that some white grains, representing the conducting material, make it both on top of, and inside, the conductive layer. Our current effort involves tracking charge deposited from the

ions and redistributing the charge to neighbor grains and adding a Poisson solver to model influence of the charge on ion trajectories.

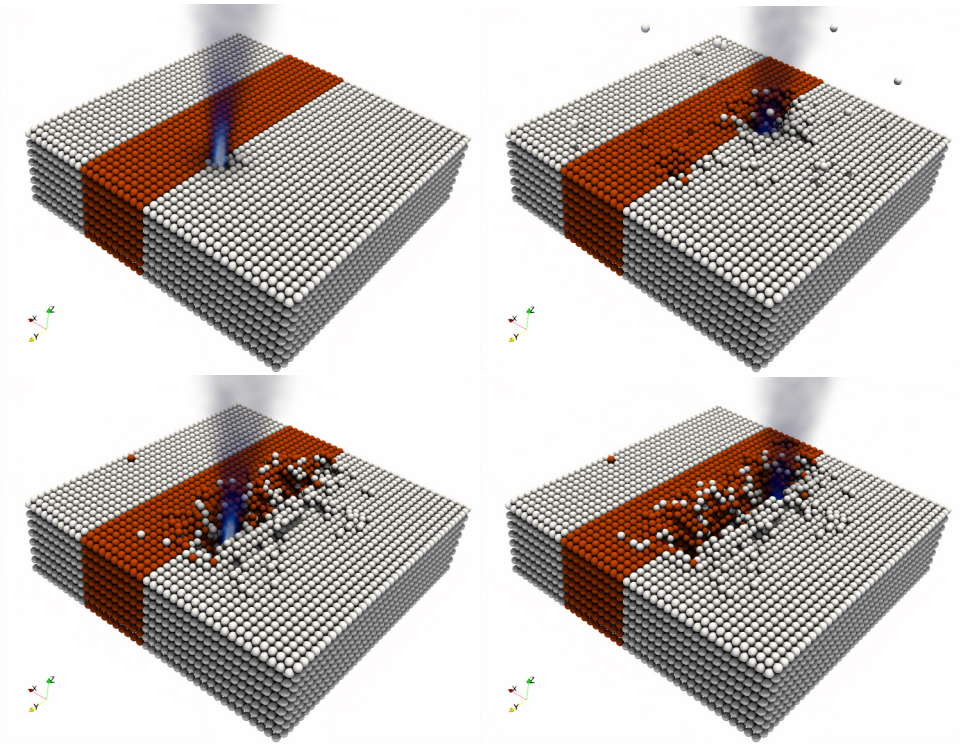

Figure 5. *Several frames from an animation demonstrating the DEM surface model*

5.CUDA Cathode Simulations

We have also developed a 1D GPU-enabled code for modeling the vacuum arc breakdown. Results from this study were presented at the 2020 ICOPS conference, Figure 6. We are seeing interesting oscillatory patterns in the charge density in cases with full ionization, that seem to be indicative of two stream instability. This effect is under investigation but if found to be physical, could be responsible for energy transfer to the ions.

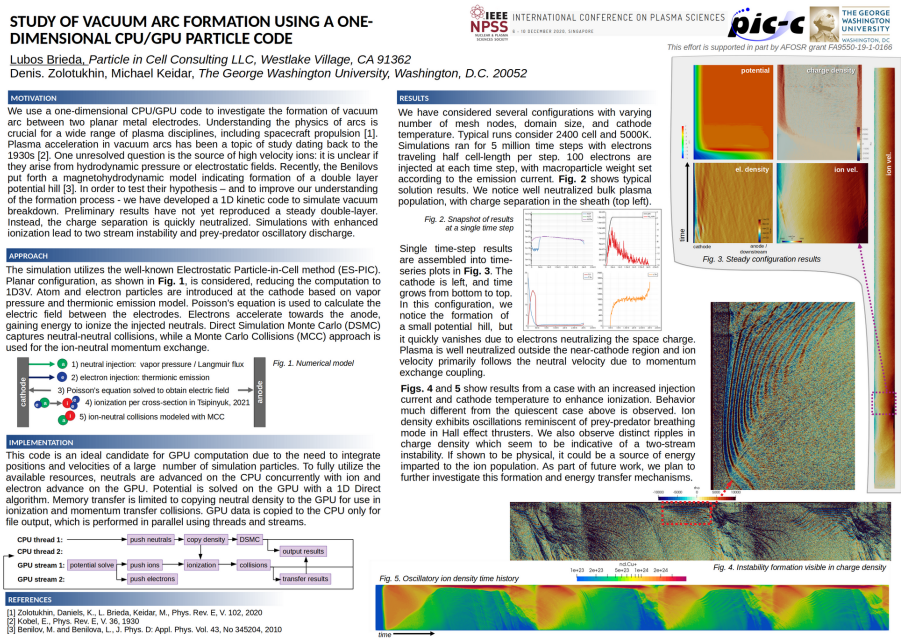

Figure 6*. Simulation of vacuum arc cathode spot formation*

6.Solenoid Field Simulation

Simulations of electron dynamics in the MPD-like vacuum arc thruster were performed. Results with a configuration with a permanent magnet is shown in Figure 7. In this configuration, electrons are strongly magnetized, leading to a JxB force at the separatrix. We have also considered a configuration with a solenoid field in which the magnetic field lines are aligned with the axis. For this configuration, we observe formation of coherent structures in the discharge electron velocity, see Figure 7 right.

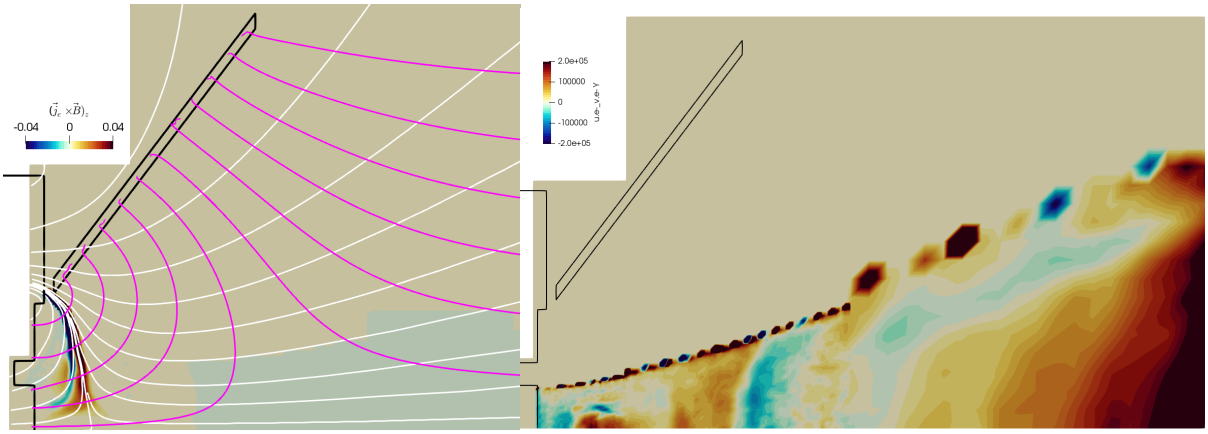

Figure 7. *JxB force with a permanent magnet field (left), and coherent structures in electron velocity with axial field (right)*

7.Simulation of Facility Effects

We have also investigated the effect of facility background pressure on the operation of Hall thrusters. Specifically, we are interested in studying the feasibility of running the device in a pulsed mode in facilities with limited pumping. The HET simulation code HPHall was modified to dynamically adjust neutral back flux according to a specified pumping speed and facility volume. By plotting the spectral response, see Figure 8, we can clearly see dampening of high frequency modes as the pressure increases. Interestingly, this behavior is similar to one observed previously by Hargus when studying chamber start up (we can expect localized high pressure due to boil off of surface-trapped water, for instance).

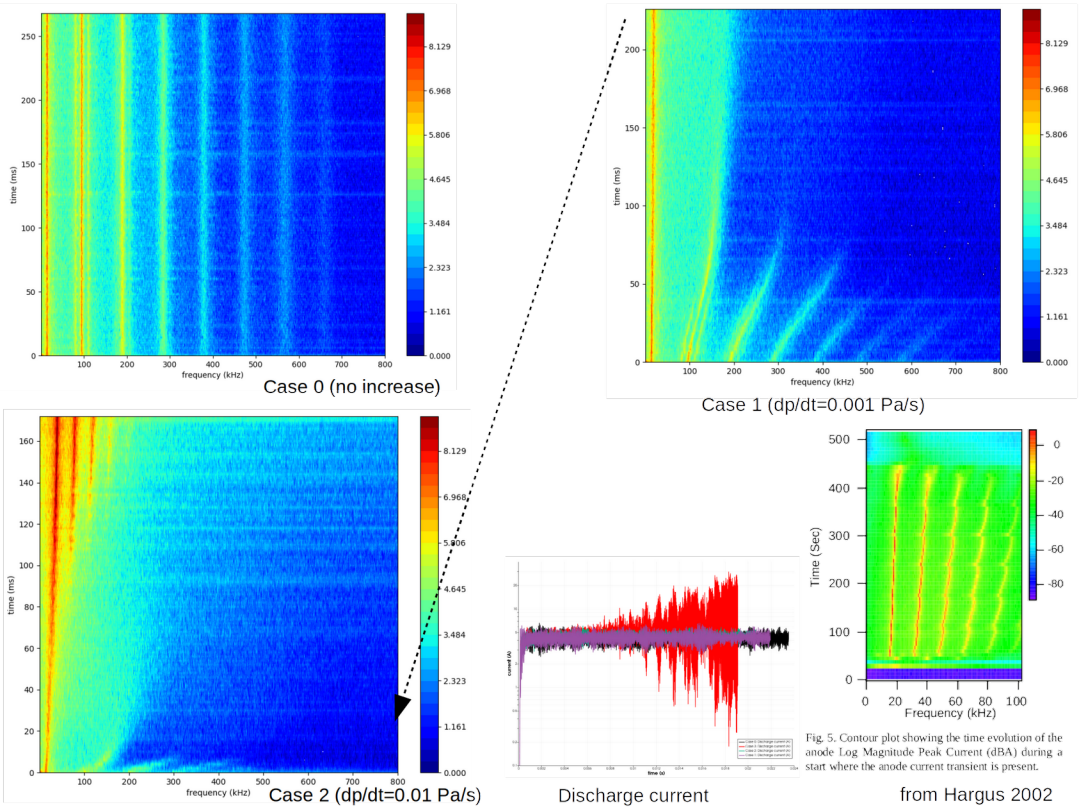

Figure 8. Temporal evolution of Hall thruster discharge current oscillations for cases with constant background pressure, and two cases with linearly increasing pressure.

We also added support for running the device in a pulsed mode in which the thruster runs for a specified number of seconds with nominal mass flow rate, followed by another period at a reduced injection. Figure 9 shows the frequency spectrum at two different pressures.

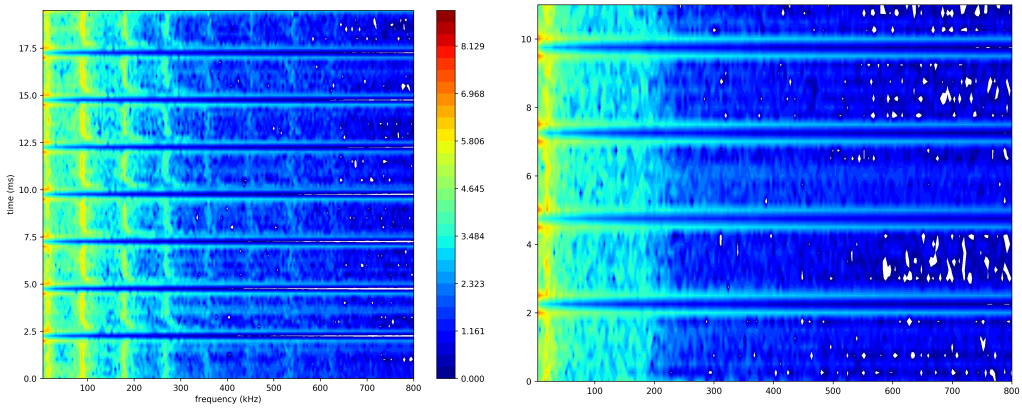

Figure 9. *Comparison of the effect of background pressure on frequency spectrum*